Applied Acoustics 164 (2020) 107244

Contents lists available at ScienceDirect

Applied Acoustics

journal homepage: www.elsevier.com/locate/apacoust

Acoustic modeling of micro-lattices obtained by additive manufacturing

Jean Boulvert [a,b,c,*], Josué Costa-Baptista [a], Théo Cavalieri [b,c], Maxime Perna [a], Edith Roland Fotsing [a], Vicente Romero-García [b], Gwénaël Gabard [b], Annie Ross [a,*], Jacky Mardjono [c,*], Jean-Philippe Groby [b,*]

[a] Laboratoire d'Analyse Vibratoire et Acoustique, LAVA, Mechanical Engineering, Polytechnique Montréal, 2900 Boulevard Edouard-Montpetit, Montréal, Québec H3T 1J4, Canada
[b] Laboratoire d'Acoustique de l'Université du Mans, LAUM – UMR CNRS 6613, Le Mans Université, Avenue Olivier Messiaen, 72085 Le Mans Cedex 9, France
[c] Safran Aircraft Engines, Villaroche, Rond Point René Ravaud – Réau, 77550 Moisy-Cramayel Cedex, France

ARTICLE INFO

Article history:
Received 10 July 2019
Received in revised form 20 January 2020
Accepted 1 February 2020
Available online 14 February 2020

ABSTRACT

The acoustic behavior of 3D printed micro-lattices is investigated to assess the impact of defects induced by the Fused Deposition Modeling technique on the parameters of the equivalent fluid medium. It is shown that the manufacturing process leads to three types of non-trivial defects: elliptical filament section, filament section shrinkage and filament surface rugosity. Not considering these defects may lead to acoustic predictions errors such as an underestimation of around 0.1 of the rigid backing absorption coefficient. Inverse characterization of seven homogeneous samples allows to fit the acoustic prediction model considering this kind of defects.

© 2020 Elsevier Ltd. All rights reserved.

1. Introduction

Additive manufacturing has proved to be a versatile and promising tool to produce sound absorbing materials. Helmholtz resonators [1], straight [2], inclined [3] and coiled tubes [1], sonic crystals [4], micro perforated panels [5] and porous treatments such as micro-lattices [6–8] are among some interesting applications. For all these acoustic materials, simple analytical models can be used to describe, analyze and optimize the geometry. Numerical or analytical models[9,10] showed that the acoustic parameters of the porous material strongly depend on several geometric parameters of the micro-structure and can be strongly affected by the manufacturing, such as change in the filaments shape of micro-lattice [11], presence of sinusoidal rugosity in micro slits [12], and surface irregularities in packed micro tubes [13]. Therefore, the impact of additive manufacturing imprecision on acoustic parameters could be very important and needs to be well described. Usually discrepancies between models and experimental results are attributed to the additive manufacturing inaccuracy or its inability to reproduce an idealized geometry [14,15].

In this work a combined numerical and experimental approach is used to describe the differences between a 3D printed micro-lattice and its idealized representation in terms of the geometry and the acoustic response. The 3D printed micro-lattices can be acoustically described by the Johnson-Champoux-Allard-Lafarge (JCAL) model [16] which accounts for the thermal and viscous losses in the effective bulk modulus and density, respectively. They are expressed in terms of air parameters and six parameters depending on the micro-structure of the porous medium. These JCAL parameters can be obtained by applying inverse characterization techniques from the measurements of the scattering coefficients of a layer of porous material. In particular, the method proposed by Niskanen et al. [17] can be used. This method is based on a statistical inversion using Bayes' formula and does not require any previous knowledge on the sample except its thickness. Moreover, in the particular case where a Representative Elementary Volume (REV) having a subwavelength scale dimension can be defined, these JCAL parameters can be also numerically computed using the Multi-Scale Asymptotic Method (MAM) [9]. In the case of periodic porous medium such as micro-lattices, the REV is the constitutive unit cell (an elementary periodic volume). Through these two techniques, the effects of the manufacturing defects on the acoustic response of the 3D printed material are analyzed. The methodology presented in this work can be extended to other 3D printed porous materials of different micro-structure or manufacturing process.

The article is organized as follows. First the micro-lattice fabrication is presented. The additive manufacturing procedure, used to create the micro-structure that governs the material acoustic behavior is detailed. Then, corresponding expected and actual micro-lattices are analyzed. The discrepancies are identified in

* Corresponding author.
E-mail addresses: jean.boulvert@univ-lemans.fr (J. Boulvert), annie.ross@polymtl.ca (A. Ross), jacky.mardjono@safrangroup.com (J. Mardjono), jean-philippe.groby@univ-lemans.fr (J.-P. Groby).

https://doi.org/10.1016/j.apacoust.2020.107244
0003-682X/© 2020 Elsevier Ltd. All rights reserved.

terms of micro-geometry differences. In the second part, the acoustic simulation and experimental characterization procedures are explained. Finally, the acoustic impact of the additive manufacturing defects is analyzed. The procedure that must be applied in order to obtain an accurate acoustic prediction model is presented.

2. Identification of the manufacturing defects

In this section, the manufacturing process and the expected resulting micro-lattices are described. Then, the manufacturing induced defects are analyzed on the basis of geometrical observations.

2.1. Additive manufacturing procedure

The Fused Deposition Modeling (FDM) *Pro2* printer supplied by *RAISE3D* is used to produce 30 mm thick cylindrical samples with a diameter of 30 mm. The extruded material is polylactic acid (PLA). The diameter of the nozzle is $D_n = 400$ µm. The revolution axis of the sample is placed vertically. The nozzle temperature is set to 200 °C; its displacement speed is 60 mm.s^{-1} and the extrusion multiplier is 0.9. The slicing software *Simplify3D* is used to generate the files providing the instructions to the printer.

The samples are printed in orthogonal direct configuration: any given micro-layer is made of parallel rods; the next micro-layer of parallel rods is orthogonal to the previous layer. This configuration is also known as "woodpile" or "interwoven perpendicular arrangement". The printer nozzle extrudes a layer of rods in the horizontal plane, then the build plate shifts vertically and allows the next orthogonal layer to be printed. The build plate displacement is set to 300 µm. This way, two consecutive orthogonal layers are separated by 300 µm and two consecutive parallel layers are separated by 600 µm. Since the filament diameter D is close to D_n, the contact between two layers is substantial as it can be seen in the idealized geometry shown in Fig. 1.

The in-plane spacing between the filaments, i.e. the lattice constant of the micro-lattice, a, can also vary. A normalized lattice parameter is defined as $A = a/D$ ($A \geqslant 1$). Samples are homogeneous if A is kept constant trough the sample's thickness, or multi-layered if A varies within the thickness. An intuitive representation of the micro-lattice would be a superposition of perfectly cylindrical parallel rods, alternating in orthogonal in-plane directions, with a 300 µm spacing between layers (Fig. 1). In this case, the rods diameter would be equal to the nozzle diameter: $D = D_n$.

The *Simplify3D* slicing software does not allow to directly control the lattice constant a. The manufacturing variable that regulates the lattice constant is the "infill factor" (*IF*). It is inversely proportional to the spacing between two adjacent filaments and can only take integer percent values. The relation between the infill factor, *IF*, and normalized lattice parameter, A, is simply obtained from the printer's instruction files and verified experimentally

$$IF(\%) = 100/A. \quad (1)$$

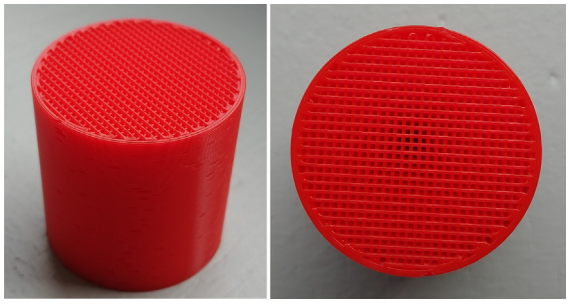

Fig. 2. Pictures of homogeneous sample.

Two pictures of a representative homogeneous sample are presented in Fig. 2. To the naked eye, the printed geometry is consistent with the idealized one. The filaments seem to be well aligned and no macroscopic defect can be seen. It is worth noting that a 800 µm thick solid layer surrounds the porous micro-lattice to provide consistency during the acoustic measurements.

2.2. Idealized representative elementary volume

From the idealized geometry (see Fig. 1), an indivisible periodic pattern, called "unit cell", can be extracted. The idealized unit cell is represented in Fig. 3. In the homogenization theory [9], the unit cell plays the role of the "Representative Elementary Volume" (REV) because the porous medium is structured in a regular pattern. More details are given below on how this theory is used to predict a porous material's acoustic behavior.

2.3. Manufacturing geometry inherent defects

The printed samples were analyzed by means of both optical microscope and scanning electron microscope (SEM) in order to identify the different possible manufacturing geometrical defects. The optical microscope has a 64× zoom and is equipped with a digital camera for the acquisition of images. The SEM produces 2D images of the sample's surface (i.e., the depth of surface irregularities cannot be assessed). The accuracy of SEM enables distinguishing details smaller than 1 µm. Samples were not coated since their conductivity was high enough to obtain high-quality images. Three types of defects were identified.

2.3.1. Filament elliptical section

Fig. 4 shows an image obtained from the optical microscope of a manually sliced sample. The image reveals two important observations. First, the filament section is not perfectly circular but rather elliptical with an horizontal major axis. The flattening of the micro-rods depends on the printing parameters. In our case, the minor axis represents in average 92% of the major axis; this leads to filament width equal to the nozzle diameter in the horizontal

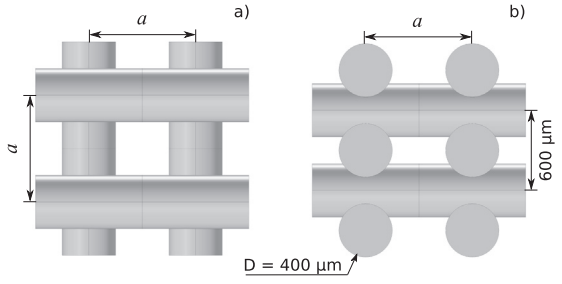

Fig. 1. Idealized geometry. a) Top view. b) Cross section.

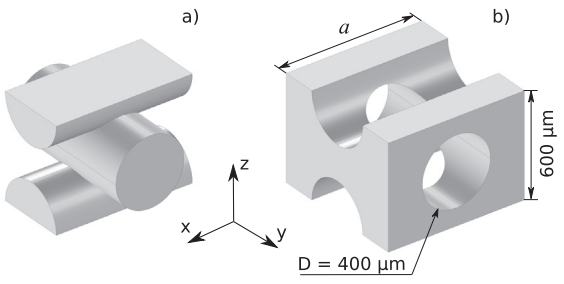

Fig. 3. Idealized Representative Elementary Volume. a) Solid phase b) Fluide phase.

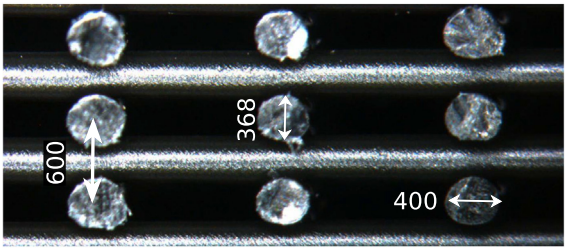

Fig. 4. Microscopic image of a micro-lattice cross section. Dimensions in micrometers.

direction (400 µm) and 92% of the nozzle diameter (368 µm) in the vertical direction. This defect does not depend on the lattice constant. The second important observation is that the spacing between two consecutive orthogonal layers is respected and is equal to 300 µm.

2.3.2. Filament section shrinkage

Due to the extrusion process, the filaments are subjected to section shrinkage. The filament is extruded by the printer then pulled by the nozzle before touching a rod from the previous layer. The shrinkage between two junctions is clearly visible as shown in Fig. 5: the section of the filaments decreases between two consecutive junctions in the direction of the material deposition. Fig. 5 shows that the widths $D1$ and $D1'$ are smaller than $D2$ and $D2'$, respectively. Empirical relations are derived to describe the minimum filament width (MFW) and the distance between the MFW position and the filament's junction with the previous orthogonal layer (MFWP). MFW and MFWP are given in micrometers, as a function of the filament step A and nozzle diameter D_n, in micrometers

$$\mathrm{MFW} = \frac{287 D_n A + 1.414 \times 10^6}{D_n A + 3391}, \quad A \in [2; 11], \tag{2}$$

$$\mathrm{MFWP} = D_n(0.8A - 1), \quad A \in [1.5; 11]. \tag{3}$$

In Fig. 5, $D1$ is a measurement of the *MFW* at the *MFWP*. These relations are used in Section IV-A to account for this manufacturing defect in the simulations. They are derived based on the microscope measurement of 10 samples with A varying between 1.5 and 11. The measurement of *MFW* is only satisfactory when A is higher than 2. Below value of lattice constant, the shrinkage is too small to be correctly measured.

2.3.3. Filament micro-grooves

The bright lines appearing on the microscopic images of micro-lattices (see Fig. 5) draw attention to nano-scale defects. The surface of the rods is not perfectly smooth. Fig. 6 shows the image of a SEM analysis revealing impurities scattered all over the filament surface. Moreover, many micro-grooves are clearly identifiable. These grooves are aligned with the filament direction.

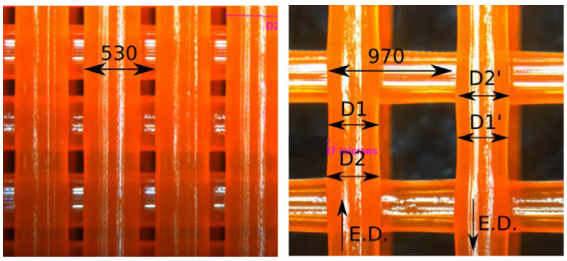

Fig. 5. Microscopic images of two micro-lattices having different lattice constant, top view. ED arrows indicate the extrusion direction. Dimensions in micrometers.

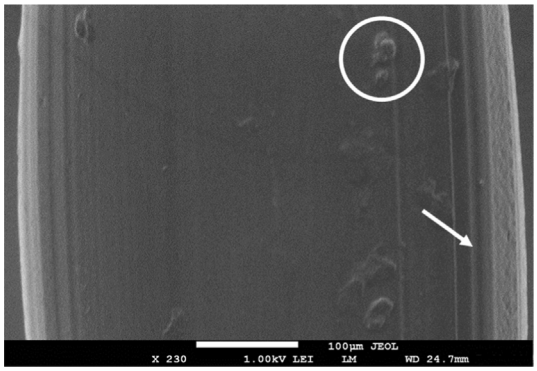

Fig. 6. SEM image of the micro-lattice, plane vue. The circle indicates an impurity and the arrow indicates a micro-groove.

Their width ranges between 5 and 20 µm. However, their exact distribution and depth could not be assessed from the SEM images. A cross-sectional view would not reveal more details of these grooves. In fact, slicing the sample always has the detrimental effect of damaging the cross-section surface of the filament. A simple explanation for the grooves origin would be that the printer nozzle's inner surface is not smooth. As a consequence, this defect might be specific to the printer nozzle and its state of wear.

FDM 3D printer nozzles are mainly made of brass, stainless and hardened steel or special materials such as ruby. The resistance to abrasion can differ from one material to another. Thus, the type and wear speed of a nozzle depend on both its constitutive material and the nature of the extruded material (PLA, Nylon...). The manufacturing technique of a nozzle also depends on the manufacturer. Among others, the shape of the hole of a brand-new nozzle depends on the drilling technique and on the type of post-drilling coating applied. Fig. 7 presents microscopic images of two new nozzles made by the same manufacturer. They are made of brass. In addition, the nozzle with a 200 µm diameter hole (Fig. 7 (c) and (d)) is plated with a nickel composite. The hole of the 200 µm nozzle is closer to a circle and has less imperfections than the other nozzle. This comparison does not benchmark manufacturers, materials or nozzle diameter but illustrates that using different nozzles certainly changes the nature of the defects of 3D printed micro-lattices.

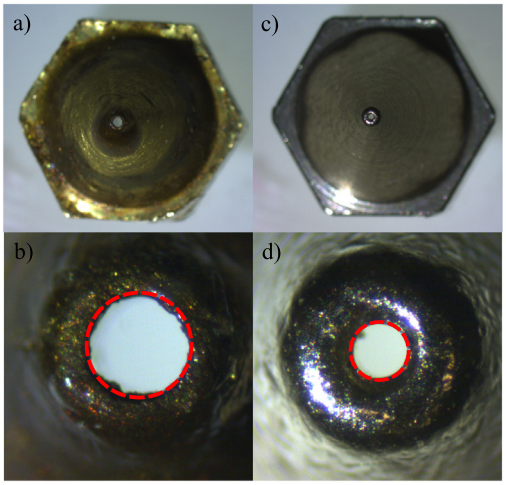

Fig. 7. Microscopic images of FDM 3D printer nozzles. a) and b) New, 400 µm diameter nozzle made from brass. c) and d) New, 200 µm diameter nozzle made from a 360 brass base material and plated with TwinClad XT coating. Red dashed circles are shown as reference. (For interpretation of the references to colour in this figure legend, the reader is referred to the web version of this article.)

3. Acoustic simulation and experimental characterization

3.1. Modeling procedure

In order to assess the impact of each defect separately, a modeling procedure is implemented. It considers the acoustic wave propagation in homogeneous and multilayer porous media as a function of microscopic parameters computed by a numerical method.

3.1.1. Acoustic model for porous media

The energy of acoustic waves penetrating a porous medium is dissipated mainly through the interaction of the wave between the frame and the pore saturating fluid (in our case air) resulting in viscous and thermal losses. If the skeleton is sufficiently dense and rigid, it can be decoupled from the air. Then, the porous medium can be considered as an equivalent fluid characterized by its complex and frequency dependent effective bulk modulus K_{eq} and density ρ_{eq}. The properties of the equivalent fluid depend on the micro-structure of the porous medium and govern its acoustic behavior [18]. There are three options to predict the properties of a porous medium's equivalent fluid. The first one consists in using empirical laws correlating a few parameters [18]. However, these laws only apply to small ranges of materials, similar to each other. The second option can be applied if the porous medium is made of aligned, non-crossing cylindrical micro-rods [4]. For this precise case, an analytical solution has been derived for porosity larger than 0.7, from a semi-phenomenological approach [18]. This kind of model is not limited to a few applications, but it requires more parameters than empirical or analytical laws. This is the case for the JCAL model [16] that provides the expression of the density and bulk modulus of the porous material as follows

$$\rho_{eq}(\omega) = \frac{\rho_0}{\phi}\alpha(\omega), \tag{4}$$

$$K_{eq}(\omega) = \frac{\gamma P_0}{\phi}\left(\gamma - \frac{\gamma - 1}{\alpha'(\omega)}\right)^{-1}, \tag{5}$$

where ω is the angular frequency, ρ_0 the density of the saturating fluid, i.e., the air medium, P_0 the static pressure, γ the specific heat ratio, ϕ the porous material porosity, $\alpha(\omega)$ its dynamic tortuosity, and $\alpha'(\omega)$ its thermal tortuosity. The two latter are defined as

$$\alpha(\omega) = \alpha_\infty - \frac{\mathrm{i}\nu}{\omega}\frac{\phi}{q_0}\sqrt{1 + \frac{\mathrm{i}\omega}{\nu}\left(\frac{2\alpha_\infty q_0}{\phi\Lambda}\right)^2}, \tag{6}$$

$$\alpha'(\omega) = 1 - \frac{\mathrm{i}\nu'}{\omega}\frac{\phi}{q_0'}\sqrt{1 + \frac{\mathrm{i}\omega}{\nu'}\left(\frac{2q_0'}{\phi\Lambda'}\right)^2}, \tag{7}$$

where $\nu = \eta/\rho_0$ is the kinematic viscosity of the saturating fluid, η its dynamic viscosity, $\nu' = \nu/Pr, Pr$ the Prandtl number, α_∞ the porous material geometrical tortuosity, Λ its viscous characteristic length, Λ' its thermal characteristic length, q_0 its visco-static permeability and q_0' its thermo-static permeability.

Once the equivalent fluid parameters are known, the acoustic behavior of the considered porous medium can be predicted. The equivalent fluid wave number k_{eq} and characteristic impedance Z_{eq} take the forms

$$k_{eq} = \omega\sqrt{\frac{\rho_{eq}}{K_{eq}}}, \tag{8}$$

$$Z_{eq} = \sqrt{\rho_{eq}K_{eq}}. \tag{9}$$

The acoustic behavior of a porous medium is then described by its six JCAL parameters: $\phi, \alpha_\infty, \Lambda, \Lambda', q_0$ and q_0'.

3.1.2. Transfer Matrix Method

The Transfer Matrix Method (TMM) is a well-known method used to predict the acoustic behavior of a monolayer or multilayer sound absorber [18]. In section V, absorption coefficients of monolayer and multilayer sound absorbers are predicted by the TMM. The transfer matrix of a porous layer is expressed in terms of its thickness, equivalent fluid wave number and characteristic impedance. The total transfer matrix of a multilayer is the product of the layers' matrices and leads to the surface impedance Z_s of the multilayer. The sound absorption coefficient $\mathcal{A}$ of a monolayer or a multilayer can be calculated by

$$\mathcal{A} = 1 - \left|\frac{Z_s - Z_0}{Z_s + Z_0}\right|^2, \tag{10}$$

where Z_0 is the acoustic impedance of the air. As stated above, the porous samples are framed by a thin solid circular wall. Its effect is considered by correcting the surface impedance by the ratio S_{sample}/S_{porous} [18]. In Eq. (10), Z_s must be replaced by Z_{s^*} defined as

$$Z_{s^*} = Z_s\frac{S_{sample}}{S_{porous}}. \tag{11}$$

The radiation effect of the solid wall is negligible.

3.1.3. Porous media: Multi-scale Asymptotic Method

In this work MAM [9] is used to numerically evaluate the JCAL parameters of a porous material made from the idealized REV. This method solves fundamental equations in the REV's fluid domain and then computes the JCAL parameters. The MAM can be implemented in a Finite Element Method (FEM) code from which the JCAL parameters are computed for any open-cell provided that the scales separation [10] is respected. It is a well suited method for the numerical evaluation of micro-geometry defects because the defects can be controlled and considered separately or simultaneously.

The MAM is implemented in the commercial FEM software *Comsol Multiphysics*. Three problems, Eqs. (12)–(14) are solved in order to retrieve the six JCAL parameters defining the porous medium's equivalent fluid when the pressure wave travels in the **z** direction (Fig. 3). The thermal problem equation, taking the limit in $\omega \to 0$, reads

$$\begin{cases} \mathrm{div}(\mathbf{grad}(\theta^0)) = -1, \\ \theta^0 = 0 \text{ on } \Gamma_{fs}, \\ \theta^0\ \Omega\ - \text{periodic}, \end{cases} \tag{12}$$

where θ^0 plays the role of the temperature field, Γ_{fs} is the fluid solid interface and Ω the REV. The visco-inertial problem, taking the limit in $\omega \to 0$, is

$$\begin{cases} \mathrm{div}(\mathbf{grad}(k_z^0)) = \frac{\partial \xi_j^0}{\partial z} - 1, \\ \frac{\partial k_z^0}{\partial z} = 0, \\ k_z^0 = 0 \text{ on } \Gamma_{fs}, \\ \langle \xi_z^0 \rangle_\Omega = 0, \\ k_z^0 \text{and} \xi^0 \Omega - \text{periodic}, \end{cases} \tag{13}$$

where $\langle\cdot\rangle_\Omega$ is the REV averaging. The visco-inertial problem, taking the limit in $\omega \to \infty$, becomes

$$\begin{cases} \frac{\mathrm{i}\omega\rho_0}{\eta}k_z^\infty = \frac{\partial \xi_z^\infty}{\partial z} - 1, \\ \frac{\partial k_z^\infty}{\partial z} = 0, \\ k_z^\infty \cdot \mathbf{n} = 0 \text{ on } \Gamma_{fs}, \\ \langle \xi_z^\infty \rangle_\Omega = 0, \\ k_z^\infty \text{ and } \xi_z^\infty\ \Omega\ - \text{periodic}, \end{cases} \tag{14}$$

where **n** is the solid surface outer normal vector. In Eqs. (13) and (14) k_z plays the role of the **z** component of the velocity field and ξ_z of its associated pressure.

The JCAL parameters are obtained by integrating the solution fields of these equations, over the fluid domain Ω_f or fluid–solid interface Γ_{fs}. They are expressed as

$$\begin{aligned}
\phi &= \frac{\int_{\Omega_f} d\Omega_f}{\int_{\Omega} d\Omega}, \quad \alpha_\infty = \phi\langle 1 - \frac{\partial \tilde{\varepsilon}_z^\infty}{\partial z}\rangle^{-1}, \\
\Lambda &= 2\frac{\int_{\Omega_f} k_z^\infty \cdot k_z^\infty d\Omega_f}{\int_{\Gamma_{fs}} k_z^\infty \cdot k_z^\infty d\Gamma_{fs}}, \quad \Lambda' = 2\frac{\int_{\Omega_f} d\Omega_f}{\int_{\Gamma_{fs}} d\Gamma_{fs}}, \\
q_0 &= \langle k_z^0 \rangle_\Omega, \quad q_0' = \frac{\int_{\Omega_f} \theta d\Omega_f}{\int_{\Omega_f} d\Omega_f}.
\end{aligned}$$

3.2. Acoustic experimental characterization

The acoustic impact of the geometry defects can be assessed numerically by means of the MAM. As a complement to this numerical approach, the samples are also characterized by using experimental acoustic techniques.

3.2.1. Acoustic direct characterization

The acoustic scattering parameters of the samples are measured using a 30 mm diameter impedance tube following the ASTME1050 and ISO 10534-2 standards. The two-microphones technique with hard backing configuration is used for the absorption coefficient measurement. The data required for the inverse characterizations (see below) are obtained using the four-microphones technique with an anechoic termination. The measurements are made between 500 Hz and 6000 Hz.

Homogeneous samples are tested in both direct and reverse orientations to make sure they are symmetric and thus, most likely homogeneous. Each sample is measured three times in both orientations. For each measurement, the sample is removed and installed again in the tube. The absorption curves are always superimposed, regardless of the measurement orientation.

3.2.2. Acoustic inverse characterization

While the MAM can be used to compute the JCAL parameters from a REV description, the measured reflection and transmission coefficients of an homogeneous porous layer can also be used to recover its JCAL parameters. Diverse methods have been discussed in the literature; in the present work, the inverse method proposed by Niskanen et al. [17] is used. To perform the procedure, a sample is tested in a four-microphones impedance tube to measure the reflection coefficient on both sides along with the transmission coefficient. During the inversion, the JCAL parameters are bounded to realistic values (eg. $\phi \in [0;1]$) and forced to respect the natural physical conditions $\Lambda \leqslant \Lambda'$ and $q_0 \leqslant q_0'$. In some cases, the reflection and transmission coefficients are strongly correlated to a subset of JCAL parameters while the other parameters have a small impact. Therefore, precise inverse characterization of the JCAL parameters is complicated. Adjusting parameters bounds to account for their prior knowledge, obtained from the numerical model, limits the field of inverse characterization research and leads to more accurate values. This way, the retrieved JCAL parameters follow realistic trends, as a function of filament spacing.

4. Effect of manufacturing defects on the JCAL parameters: numerical evaluation

Three types of defects inherent to additive manufacturing been identified. It is suspected that their impact on the acoustic response depends on the spacing of the rods. In this section, their impact is numerically studied for the range of $A \in [1.2;25]$.

4.1. Elliptical section and section shrinkage

The impact of the elliptical section and shrinkage of the filaments are analyzed in this section by modifying the idealized REV. The micro-lattice composed of 400 µm perfectly cylindrical rods is taken as a reference. The considered elliptical section has a 368 µm vertical minor axis and a 400 µm horizontal major axis. The geometry of the shrinkage is described by Eqs. (2) and (3). Fig. 8(a) shows the meshed REV used in these calculations. An example of the visco-static MAM field is given in Fig. 8(b) and (c) for the case of perfectly cylindrical and elliptical rods, respectively. This field is used to compute the viscous permeability q_0.

The section shrinkage is negligible when A is lower than 2 and is then not accounted for in the unit cell. The impacts of the defects are summarized in Table 1 with the following main findings:

- the elliptical filament section significantly increases the porosity ϕ and permeabilities q_0 and q_0' when the filaments are very close to each other, and slightly increases the thermal length Λ'.

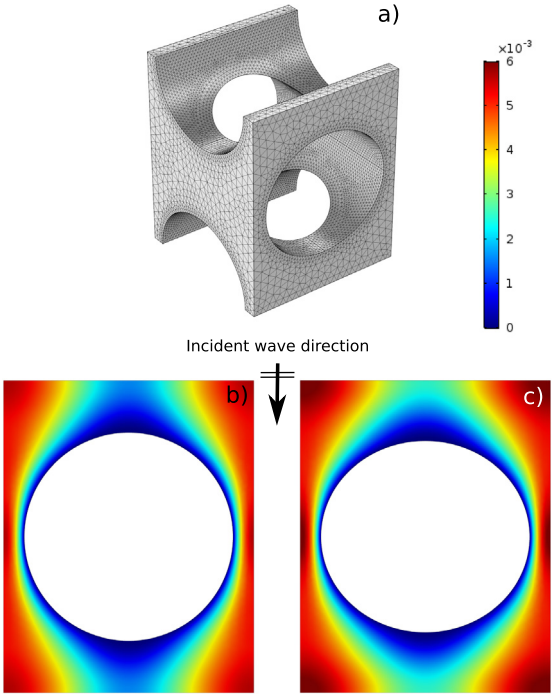

Fig. 8. 3D micro-lattice MAM visco-static simulation with $A = 1.2$. a) Unit cell. b) Velocity field component in incident wave direction, with cylindrical rods. c) Velocity field component in incident wave direction, with elliptical rods. The vertical minor axis is equal to 92% of the horizontal major axis.

Table 1
JCAL parameters relative difference (%) with respect to perfectly cylindrical rods. Data obtained from FEM numerical simulations. A positive value indicates that the corresponding defect increases the considered JCAL parameter, and vice versa.

Defect	A	ϕ	α_∞	Λ	Λ'	q_0	q_0'
Elliptic	1.2	15	2	0	5	19	22
	10	1	0	0	4	3	1
	25	0	0	0	4	2	0
Shrinkage	10	1	0	1	9	4	5
	25	1	1	0	12	2	2
Elliptic and Shrinkage	1.2	15	2	0	5	19	21
	10	2	0	1	13	5	6
	25	1	0	0	17	2	3

Fig. 8(b) and (c) show that the volume occupied by the filaments is slightly smaller when their section is elliptical. Moreover, looking at the color map, the velocity field component in incident wave direction surrounding the cylindrical rods seems higher than the one surrounding the elliptical rods. Both observations are coherent with the fact that the porosity and viscous permeability are higher when considering elliptical filaments;

- the filament section shrinkage increases the thermal length Λ' when the filaments are far from each other and therefore the shrinkage is strong (see Eq. (2));
- the combination of both defects results in a significant increase of the porosity ϕ and permeabilities q_0 and q_0' when the filaments are very close to each other. Moreover, an increase of the thermal length Λ' is achieved when the filament spacing is large.

4.2. Micro grooves

In order to study the effect of the presence of the micro grooves on the acoustic parameters, a simple 2D model is developed. The grooves are not implemented in a 3D model because of exceptionally long computation time related to the necessary fine mesh size of the grooves. The REV for the 2D case is shown in Fig. 9(a). In reality, the distribution of grooves seems random and their depth could not be measured precisely. Here, we consider rods of diameter D equally spaced by a distance $D \times A$ in which periodic grooves are added to the rods surface (see Fig. 9(b) and (c)). As many arbitrary choices and simplifications are made, the aim of this simulation is to assess the general physical trend. Note that fillets at the corners of the grooves are required to respect MAM surfaces conditions, and thus avoid any singularity in the resolution of the high-frequency limit of the visco-inertial problem, Eq. (14).

Fig. 9 shows the dimensions of the geometry, the converged mesh and the visco-inertial MAM velocity field. The latter is used to compute the viscous length Λ. On the one hand, the porosity ϕ, tortuosity α_∞, viscous q_0 and thermal q_0' permeabilities are not affected by the grooves, or very little when A is close to 1.2. Then, their relative variations are 5%, 1%, 4% and 4% respectively. On the other hand, the characteristic lengths Λ and Λ' are impacted by the grooves. Λ is reduced by 16% while Λ' is reduced by 26%. These variations are constant except when A is close to 1.2. The variation of Λ' was expected as it is defined by the ratio of the fluid volume over the fluid-skeleton surface [18]. Thus, the presence of grooves leads to the variation of the fluid-skeleton surface without changing the fluid volume, except when the rods are very close to each other and the porosity is affected by the grooves. The JCAL parameters variations with respect to the idealized REV are summarized in Table 2.

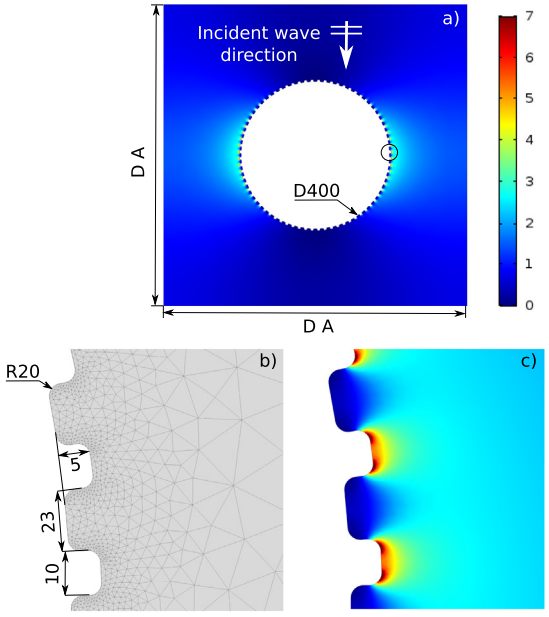

Fig. 9. Grooved filament 2D MAM simulation. a) Unit cell and visco-inertial, $\omega \to \infty$, MAM velocity field. b) Grooves geometry and mesh. c) Visco-inertial, $\omega \to \infty$, MAM velocity field detail. All dimensions are in microns.

5. Effect of Manufacturing defects on the JCAL parameters: experimental evaluation

The defects inherent to additive manufacturing have been numerically studied. In this section, their impact is experimentally studied for the range of $A \in [1.4; 6.7]$, along with that of potentially non identified defects.

5.1. Experimentally corrected model

Seven homogeneous samples are used to obtain the experimentally corrected model describing the variation of the JCAL parameters with respect to the infill factor, *IF*, and thus to the normalized lattice parameter A. The printer nozzle diameter is $D_n = 400$ µm. *IF* takes the values {15, 22, 30, 40, 50, 60, 70}% (i.e., $A \in [1.43; 6.67]$). Homogeneous samples with either significantly larger or smaller values for A have a low absorption coefficient which complicates their inverse characterization. Such samples are of low practical interest for noise control applications.

For each sample, an inverse characterization is performed in order to retrieve the JCAL parameters from experiments. The JCAL parameter bounds are set around the FEM values of the unit cell with elliptical rods section and no shrinkage. The grooves should significantly reduce the characteristic lengths while the filaments shrinkage should affect porosity, thermal length and permeabilities. During the inverse characterization process, the characteristic lengths can vary between 1.1 and 1/3 times the unit cell values. The porosity ϕ and tortuosity α_∞ could vary between ± 0.1 of the unit cell value, and permeabilities q_0 and q_0' are ranged between 3 and 1/3 time the values of the unit cell.

Inverse characterization of the homogeneous samples leads to the JCAL parameters corresponding to certain infill factors. To obtain a complete parametric model linking the JCAL parameters to the infill factor, piece-wise cubic interpolations (*Matlab, cubicinterp*) of the data was processed for the seven homogeneous samples. Simple analytic expressions of the variation of the JCAL parameters with respect to the infill factor could not be derived without important loss of accuracy.

Fig. 10 presents the parametric model of the JCAL parameters with respect to the infill factor. The values obtained during inverse characterization and the interpolated curves defining the experimentally corrected JCAL parameters model are shown along with the values for the idealized REV and the authorized research scope.

Table 2
JCAL parameters relative difference (%) of grooved rods with respect to perfectly circular rods. Data obtained from 2D numerical simulations. A positive value indicates that the corresponding defect increases the considered JCAL parameter, and vice versa.

Defect	A	ϕ	α_∞	Λ	Λ'	q_0	q_0'
Grooves	1.2	5	1	−14	−24	4	4
	10	0	0	−16	−26	0	0
	25	0	0	−16	−26	0	0

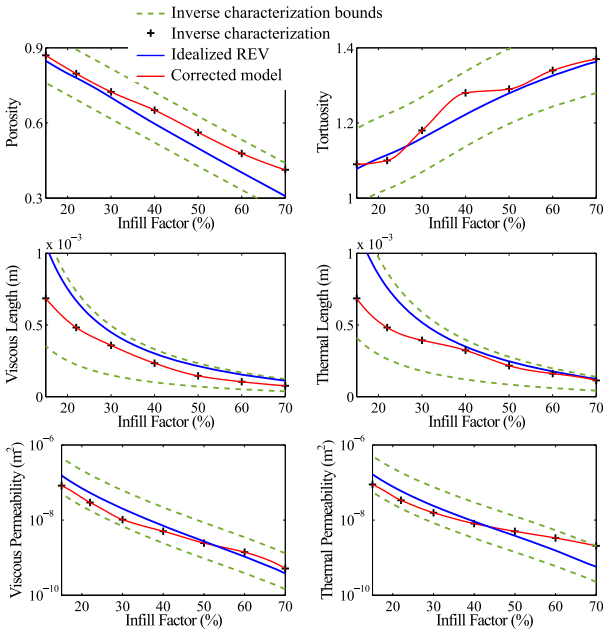

Fig. 10. JCAL parametric model with respect to the infill factor, considering idealized REV (blue line), from inverse characterization of homogeneous samples (red line). The green dashed lines indicates the authorized research scope during inverse characterization. The black markers spot the inverse characterization values. (For interpretation of the references to colour in this figure legend, the reader is referred to the web version of this article.)

The trends of the experimental JCAL parameters with respect to the infill factor are similar to those considering idealized REV. In details, it can be noted that:

- The values of the porosity obtained experimentally are higher than those obtained numerically using the idealized REV. The difference is more marked when the infill factor is high, i.e., the lattice constant is low. It is 27% higher for $IF = 70\%$. This effect was already observed during the numerical study.
- The tortuosity is fairly well predicted numerically considering the idealized REV, which is in accordance with the simulations of the defects. The biggest shift is observed for $IF = 40\%$ where the experimentally retrieved tortuosity is only 0.06 higher than that of the idealized REV. Such difference of tortuosity has only a small impact on the acoustic response of a porous material.
- The experimental characteristic lengths are lower than those obtained numerically considering the idealized REV. The viscous length is on average 30% lower experimentally and the shift is almost constant. A near constant down-shift was numerically predicted and is due to the presence of grooves on the filaments surface.

  The experimental thermal length is close to the one obtained numerical considering idealized REV for medium and high infill factors, i.e., medium and low lattice constants. Moreover, for $IF = 15\%$, the experimental one is 40% lower. The simulations of the defects suggest that the down-shifting of the thermal length caused by the presence of grooves on the filaments surface may be partially compensated by elliptical and shrinked filament section for high lattice constant; which is not the case however.
- The permeabilities were predicted to be higher in presence of defects, especially for low lattice constant. This forecast is experimentally confirmed. For $IF = 70\%$ the experimental viscous permeability is 15% higher than the one numerically predicted considering an idealized REV and the thermal permeability is 3 times higher. However, for high lattice constant, the trend is inverted. For $IF = 15\%$ both experimental permeabilities are 45% lower. It is worth noting that any permeability higher than $\approx 2 \cdot 10^{-8}$ m^2 will give overlaid absorption curves, providing all other JCAL parameters are kept constant. Thus, the permeabilities obtained from inverse characterization of the high lattice constant samples ($IF < 30\%$) should be viewed with caution.

For illustration, the JCAL parameters of two homogeneous samples used for the inversion process ($IF = 50\%$, i.e., $A = 2$ and $IF = 30\%$, i.e., $A = 3.33$) are summarized in Table 3 considering the values from idealized micro-structure simulation, and in Table 4 considering values from inverse characterization. The absorption coefficients of these samples are presented in Fig. 11. As described in Ref. [14], the measured absorption coefficient is up to 0.1 higher than the coefficient simulated considering idealized micro-structure. Both curves follow the same trend. Still, the disparity between measured and simulated absorption coefficients is not the unique consequence of acoustic measurement imprecision. It is evidenced that the measured acoustic absorption coefficients of homogeneous samples do not match the simulations with idealized micro-structure, and it is clear that the printed geometry differs from the idealized simulated one, which causes important acoustic discrepancies.

Finally, the inverse characterization gives very satisfactory results for three reasons. First, the JCAL parameters retrieved from inverse characterization follow realistic monotonic trends (Fig. 10). Second, the shifting of the JCAL parameters due to the presence of

Table 3
JCAL parameters of homogeneous samples, numerically computed considering the idealized REV. D = 400 μm.

A	ϕ	α_∞	Λ (μm)	Λ' (μm)	$q_0(10^{-9}$ m$^2)$	q_0' $(10^{-9}$ m$^2)$
2	0.51	1.28	217	252	2.89	4.05
3.33	0.71	1.16	447	515	20.0	23.7

Table 4
JCAL parameters of homogeneous samples, from inverse characterization. D_n = 400 μm.

IF(%)	ϕ	α_∞	Λ (μm)	Λ' (μm)	q_0 $(10^{-9}$ m$^2)$	$q_0'(10^{-9}$m$^2)$
50	0.56	1.29	145	216	2.45	5.02
30	0.72	1.18	358	393	10.3	15.7

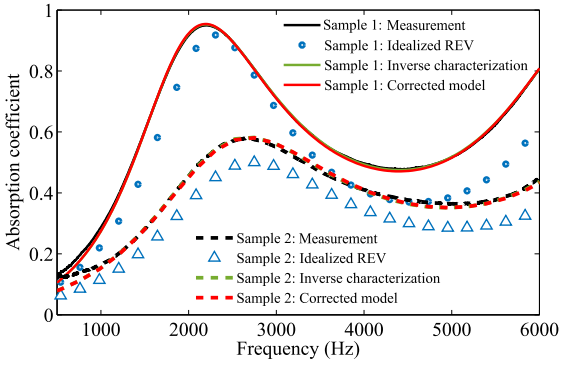

Fig. 11. Hard backed absorption coefficient measured (black lines), simulated considering the idealized geometry (markers), obtained from inverse charcaterization (green lines) and from the corrected model (red) of two homogeneous samples. Sample 1: $IF = 50\%$, i.e., $A = 2$. Sample 2: $IF = 30\%$, i.e., $A = 3.33$. (For interpretation of the references to colour in this figure legend, the reader is referred to the web version of this article.)

defects is oriented in the same direction numerically and experimentally. Third, the obtained absorption curves are almost perfectly overlaid to the measurement curves, when considering the JCAL parameters either from inverse characterization or from the corrected parametric model (Fig. 11).

5.2. Validation

To validate the corrected predictive model, one bi-layers ($IF = [60, 30]\%$, i.e., $A = [1.67, 3.33]$), one three-layers ($IF = [44, 55, 33]\%$, i.e., $A = [2.27, 1.82, 3.03]$) and one six-layers ($IF = [15, 25, 35, 45, 55, 65]\%$, i.e., $A = [6.67, 4.00, 2.86, 2.22, 1.82, 1.54]$) samples were printed and simulated by the TMM. It should be noted that some of the considered multilayers IF do not belong to the set of homogeneous samples IF used for the inverse characterization.

Each sample was printed in one step. Fig. 12 presents the absorption coefficient measured and predicted on both sides of the multilayer samples. The bi-layer sample is composed of two 15 mm thick layers, the three-layers sample is composed of three 10 mm thick layers and the six-layers sample is composed of six 5 mm thick layers. It can be observed that the model considering idealized REV do not fit well the measured absorption coefficients while the experimentally corrected model, (Fig. 10), is in very good agreement with the experimental values.

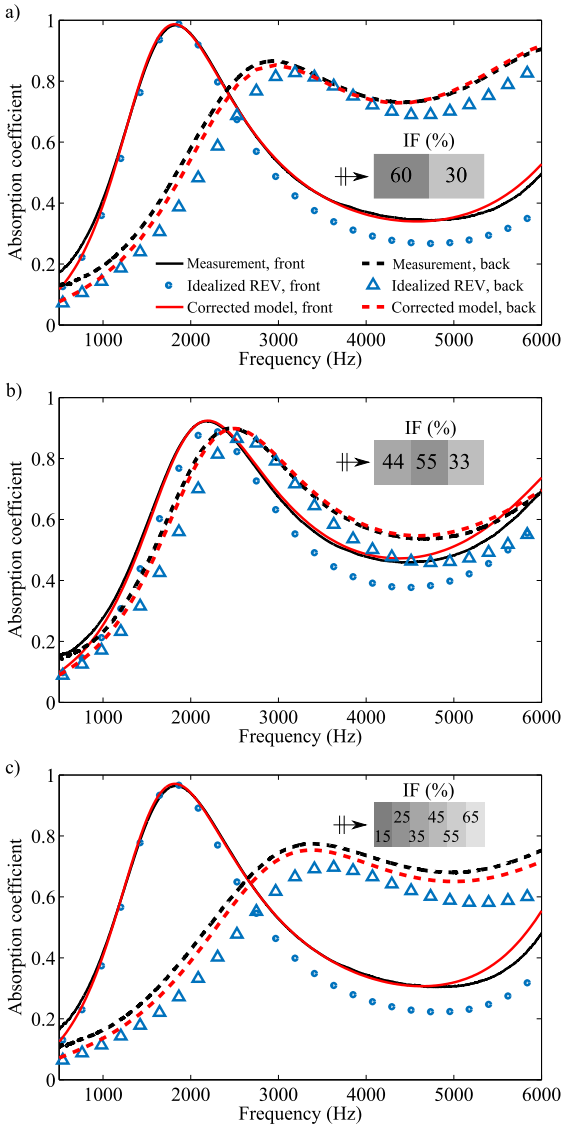

Fig. 12. Hard backed absorption coefficient of 30 mm thick multilayers, $D_n = 400$ µm, samples, measured (black lines) and simulated without considering the defects (blue marks) and simulated by the experimentally corrected model (red lines) on both sides. a) $IF = [60, 30]\%$. b) $IF = [44, 55, 33]\%$. c) $IF = [15, 25, 35, 45, 55, 65]\%$. (For interpretation of the references to colour in this figure legend, the reader is referred to the web version of this article.)

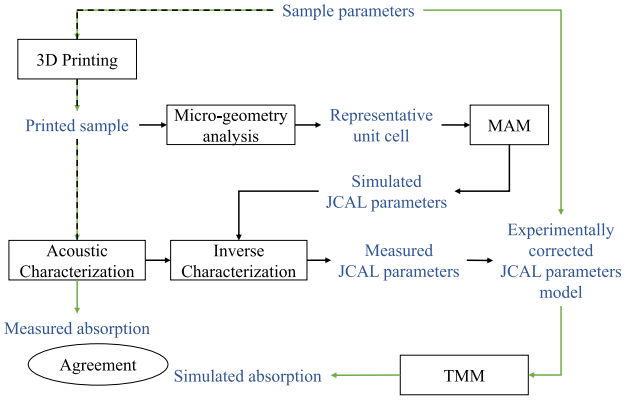

Fig. 13. Routine diagram. Following the black lines leads to experimentally corrected JCAL parameters variation with respect to the considered sample parameter. Green lines indicate how to confirm the accuracy of the corrected model. (For interpretation of the references to colour in this figure legend, the reader is referred to the web version of this article.)

5.3. Accurate JCAL parametric model routine

The approach to account for the impact of the geometry defects is summarized in Fig. 13. It can be applied to other porous materials and to other manufacturing techniques. It consists in simulating the JCAL parameters of the unit cell using the MAM. Experimental geometric and acoustic measurements, including inverse characterization of homogeneous samples, provide the parametric model. Defects that can be simply and accurately described, such as elliptical section or filament section shrinkage, can be accounted for in the definition of the unit cell, while complicated or random defects such as grooves are considered by tuning the equivalent fluid parametric model. Prior knowledge of the parameters scopes simplifies the experimental retrieval of realistic JCAL parameters values.

TMM with the corrected model is applied to multilayered samples and compared to experimental results in order to validate the routine.

6. Conclusion

In this work, the discrepancies between an idealized micro-lattice and its actual geometry have been discussed. Considering a simple model enables a rough prediction of the acoustic behavior. However, neglecting the micro-geometric defects such as elliptical section, section shrinkage or micro-grooves reduces the accuracy of the model. The effect of each defect has been detailed in terms of JCAL parameters. Some of them depend on the filament spacing, especially when the spacing is very small. An experimental fitting routine based on prior knowledge of the parameters scopes can easily be performed to best fit with the experimental values of the sound absorption measurements. The very good experimental agreement with the corrected model pave the way to optimally graded porous material [19].

This work focused on FDM 3D printed micro-lattices. Yet, micro-geometric defects are not exclusive to this kind of porous material or this additive manufacturing technique in particular.

The routine leading to an accurate model can be applied to other porous materials made by other 3D printing processes such as stereolithography or selective laser melting.

Moreover, micro-geometric defects are most probably device-dependent. In other words, two synchronized printers of the same model, might not manufacture samples having the same acoustic parameters. In a similar fashion, the micro-geometric defects might be dependent on device wear.

CRediT authorship contribution statement

Jean Boulvert: Conceptualization, Methodology, Software, Validation, Formal analysis, Investigation, Resources, Writing - original draft, Writing - review & editing, Visualization. **Josué Costa-Baptista:** Methodology, Investigation, Resources. **Théo Cavalieri:** Conceptualization, Methodology, Software, Validation. **Maxime Perna:** Methodology, Investigation. **Edith Roland Fotsing:** Conceptualization, Methodology, Formal analysis, Investigation, Writing - review & editing, Supervision. **Vicente Romero-García:** Methodology, Investigation, Visualization, Supervision. **Gwénaël Gabard:** Writing - review & editing, Supervision, Project administration, Funding acquisition. **Annie Ross:** Conceptualization, Writing - review & editing, Supervision, Project administration, Funding acquisition. **Jacky Mardjono:** Conceptualization, Supervision, Project administration, Funding acquisition. **Jean-Philippe Groby:** Conceptualization, Software, Formal analysis, Investigation, Writing - original draft, Writing - review & editing, Supervision.

Declaration of Competing Interest

The authors declare that they have no known competing financial interests or personal relationships that could have appeared to influence the work reported in this paper.

Acknowledgments

The authors acknowledge Safran Aircraft Engines, the Natural Sciences and Engineering Research Council of Canada (NSERC) for supporting and funding this research. They acknowledge financial support from ANR industrial chair MACIA (ANR-16-CHIN-0002). They also would like to thank L. Schwan for useful discussion on homogenization theory.

References

[1] Cai X, Guo Q, Hu G, Yang J. Ultrathin low-frequency sound absorbing panels based on coplanar spiral tubes or coplanar Helmholtz resonators. Appl Phys Lett 2014;105:121901.
[2] Jiang C, Moreau D, Doolan C. Acoustic Absorption of Porous Materials Produced by Additive Manufacturing with Varying Geometries, in Sound, Science and Society (Perth, 2017). p. 8..
[3] Liu Z, Zhan J, Fard M, Davy JL. Acoustic properties of a porous polycarbonate material produced by additive manufacturing. Mater Lett 2016;181:296–9.
[4] Guild MD, Garcia-Chocano VM, Kan W, Sanchez-Dehesa J. Acoustic metamaterial absorbers based on confined sonic crystals. J Appl Phys 2015;117:. arXiv: 1405.7200114902.
[5] Liu Z, Zhan J, Fard M, Davy JL. Acoustic properties of multilayer sound absorbers with a 3d printed micro-perforated panel. Appl Acoust 2017;121:25–32.
[6] Fotsing ER, Dubourg A, Ross A, Mardjono J. Acoustic properties of periodic micro-structures obtained by additive manufacturing. Appl Acoust 2019;148:322–31.
[7] Cai X, Yang J, Hu G, Lu T. Sound absorption by acoustic microlattice with optimized pore configuration. J Acoust Soc Am 2018;144:EL138–43.
[8] Guild MD, Rothko M, Sieck CF, Rohde C, Orris G. 3d printed sound absorbers using functionally-graded sonic crystals. J Acoust Soc Am 2018;143. 1714–1714.
[9] Auriault J-L, Boutin C, Geindreau C. Homogenization of coupled phenomena in heterogenous media; 2009. oCLC: 733729827..
[10] Lee C-Y, Leamy MJ, Nadler JH. Numerical calculation of effective density and compressibility tensors in periodic porous media: a multi-scale asymptotic method. In Comsol Conference (Boston, 2008). p. 6..
[11] Venegas R, Umnova O. On the influence of the micro geometry on sound propagation through periodic array of cylinders. J Acoust Soc Am 2008;123. 3142–3142.
[12] Song SY, Yang XH, Xin FX, Ren SW, Lu TJ. Modeling of roughness effects on acoustic properties of micro-slits. J Phys D: Appl Phys 2017;50:235303.
[13] Kulpe JA, Lee C-Y, Leamy MJ. Computation of acoustic absorption in media composed of packed microtubes exhibiting surface irregularity. J Acoust Soc Am 2011;130:826–34.
[14] Zielinski. Pore-size effects in sound absorbing foams with periodic microstructure: modelling and experimental verification using 3d printed specimens. In ISMA 2016 -International Conference on Noise and Vibration Engineering (Leuven, 2016). p. 11..
[15] Deshmukh S, Ronge H, Ramamoorthy S. Design of periodic foam structures for acoustic applications: concept, parametric study and experimental validation. Mater Design 2019;175:107830.
[16] Lafarge D, Lemarinier P, Allard J, Tarnow V. Dynamic compressibility of air in porous structures at audible frequencies. J Acoust Soc Am 1997;102:1995–2006.
[17] Niskanen M, Groby J-P, Duclos A, Dazel O, Le Roux JC, Poulain N, Huttunen T, Lahivaara T. Deterministic and statistical characterization of rigid frame porous materials from impedance tube measurements. J Acoust Soc Am 2017;142:2407–18.
[18] Allard J-F, Atalla N. Propagation of sound in porous media: modelling sound absorbing materials. 2nd ed. Hoboken, N.J.: Wiley; 2009.
[19] Boulvert J, Cavalieri T, Costa-Baptista J, Schwan L, Romero-García V, Gabard G, Fotsing ER, Ross A, Mardjono J, Groby J-P. Optimally graded porous material for broadband perfect absorption of sound. J Appl Phys 2019;126:175101.